Author's Accepted Manuscript

Fracture toughness of a hot work tool steel-TiC composite produced by mechanical milling and Spark Plasma Sintering

Sebastian Henschel, Volodymyr Kietov, Faraz Deirmina, Massimo Pellizzari, Lutz Krüger

Cite this article as: Sebastian Henschel, Volodymyr Kietov, Faraz Deirmina, Massimo Pellizzari and Lutz Krüger, Fracture toughness of a hot work tool steel-TiC composite produced by mechanical milling and Spark Plasma Sintering, *Materials Science & Engineering A,* https://doi.org/10.1016/j.msea.2017.10.053

Fracture toughness of a hot work tool steel-TiC composite produced by mechanical milling and Spark Plasma Sintering

Sebastian Henschel[a,*], Volodymyr Kietov[a], Faraz Deirmina[b], Massimo Pellizzari[b], Lutz Krüger[a]

[a] Institute of Materials Engineering, TU Bergakademie Freiberg, Gustav-Zeuner-Str. 5, 09599 Freiberg, Germany

[b] Department of Industrial Engineering, University of Trento, via Sommarive 9, 38123 Trento, Italy

* Corresponding author: sebastian.henschel@iwt.tu-freiberg.de

Abstract

The effect of the processing route and the addition of 20 Vol% TiC particles on the fracture toughness of the hot work tool steel AISI H13 was investigated. To this end, as-atomized, mechanically milled and mechanically alloyed powders were consolidated by spark plasma sintering. Nearly dense materials were produced. The fracture toughness was measured with modified disk-shaped compact tension specimens. Acoustic emissions and the fracture surfaces were analyzed to study the damage evolution. The consolidation of the as-atomized powder resulted in the highest relative density and fracture toughness. In contrast, relatively low fracture toughness was achieved for the mechanically milled powder which was attributed to the lower relative density after sintering. The lowest fracture toughness was achieved for the steel-TiC composite material that also exhibited the lowest density. Furthermore, crack path deflection was lowest for this material. This was attributed to the TiC particles which served as a weak crack path. Early cleavage fracture due to stress concentration at TiC particles/agglomerations was proved by means of acoustic emission analysis.

Keywords: AISI H13, hot work tool steel, metal matrix composite, titanium carbide, spark plasma sintering, fracture toughness

1. Introduction

Hot work tool steels are widely used for die forging or die casting tools. Due to the complex shape of such tools, not only the strength but also the fracture toughness of the materials is critical for the application. The high metallurgical cleanliness required for tool steels (i.e. low amount of non-metallic inclusions, low segregation) implies the use of complex melting and remelting practices like electroslag- (ESR) and vacuum arc remelting (VAR). The production by means of powder metallurgy (PM), typically by hot isostatic pressing (HIP), results in a relatively fine carbide distribution, fine grain size, uniformity, and cleanliness [1].

In most recent years, with the advent of fast sintering techniques, new efforts have been made to further improve the microstructure and the properties of PM tool steel, especially after preliminary mechanical milling. Pellizzari et al. [2–4] investigated the densification behavior

1

of AISI H13 with different particle size distributions during spark plasma sintering (SPS). For gas atomized powder with a wide particle size distribution a relative density of 99.4 % was achieved. A higher relative density of 99.6 % was obtained for a smaller powder particle size of < 45 μm. These materials were sintered at 1100 °C for 5 min. Finer particles which were produced by mechanical milling (MM) resulted in a relative density of 99.5 % after sintering for 1 min at 1100 °C.

Due to the large surface area of fine powders, an oxide surface layer can form. This contamination does not affect the densification. However, the bonding strength between the particles and the toughness are significantly decreased [3].

Hard particle (HP) reinforcement is a suitable way to improve the hardness and wear resistance of mechanically milled tool steel, due to the combined effects of dispersion hardening by HP and strain hardening by severe plastic deformation during MM. Fedrizzi showed that TiC does not react with AISI H13, thus providing good chemical stability during SPS at 1100 °C [5]. The hardness increased from 425 HV10 for the pure MM AISI H13 to 825 HV10 for mechanically alloyed (MA) AISI H13 with 20 %vol TiC. The TiC particles decrease the densification rate so that a holding time of 30 min at 1100 °C was necessary to achieve maximum densification (99.4 %).

The *apparent* fracture toughness K_{app} of the unreinforced tool materials was determined by means of a customary test method developed for small notched specimens [6]. It was determined with single edge-notched bend (SENB) bars with an electro discharge machined (EDM) notch with a notch root radius of $r = 50$ μm. Due to the relatively low stress triaxiality, the measured K_{app} is larger than the plane-strain fracture toughness K_{Ic}. Typical K_{Ic} values determined for large-sized fatigue pre-cracked samples, range between 25 and 50 MPa m$^{0.5}$ [7–10]. Table 1 shows the apparent fracture toughness for these materials.

Table 1. Apparent fracture toughness of spark plasma sintered AISI H13.

Powder	Density / %	HV10	K_{app} / MPa m$^{0.5}$	Reference
AT	99.4	425	75	[4]
MM	99.5	475	57	[4]

Pezzotti et al. [11] studied crack growth in Al_2O_3 and Si_3N_4 ceramics reinforced with SiC. Crack growth prior to catastrophic failure was detected by analyzing the acoustic emissions. It was observed that the particle reinforcement resulted in crack bridging and pop-in events. Acoustic emission analysis is also a suitable method to detect the damage processes before the failure in high-strength steels. Ingham et al. [12] observed a rapid increase in acoustic emissions count rate immediately prior to fracture of a 300M high strength steel. Analogously, Lambert et al. [13] detected high-energy acoustic events before fracture of high-strength low-alloy steels. These results were attributed to the formation of microcracks. For AISI 1060 and 1080 steels, Roy et al. [14] showed that high-energy acoustic events can be related to the formation of pop-ins.

2

In spite of the large amount of papers dealing with the strength and ductility of ultrafine grained (UFG) and nanocristalline (NC) materials, less attention has been paid to their fracture toughness. This is of particular importance for high strength materials, because in presence of long cracks ($a > K_{Ic}^2/(\pi\sigma_y)$) the fracture strength becomes directly controlled by the critical stress intensity factor, K_{Ic} [15].

In this paper, the plane strain fracture toughness of spark plasma sintered AISI H13 is compared to those of the same tool steel, mechanically milled (MM) and mechanically alloyed (MA) with 20 Vol% TiC. The fracture behavior is described as a function of the grain shape, which is elongated after milling. The damage evolution is evaluated by analysis of acoustic emissions and by fractography.

2. Materials and methods

Gas atomized powder of the hot work tool steel AISI H13 (manufacturer Sandvik Osprey, 0.45 % C, 1.62 % Mo, 5.36 % Cr, 1.1 % V, 0.43 % Mn, 0.94 % Si, Fe bal.) was used in the present work. The particles size distribution of the as-atomized powder (AT) is given by: $d_{10} = 19$ μm, $d_{50} = 31$ μm, $d_{90} = 51$ μm. The mean particles size of the TiC powder is 3 μm.

The powders to be milled (Table 2) were mixed with 0.2 wt% Kenolube (Hoganas AB) in a Turbula mixer for 60 min. The premixed batch of powder was then mechanically milled (MM) using a Fritsch Pulverisette 6 planetary ball mill. The total milling time was 200 min with 100 cycles of 2 min milling and 9 min pause in order to reduce the temperature increase during the milling. Steel balls (100Cr6, 65 HRC, $d = 10$ mm) were used with a ball to powder ratio of 10:1.5 (6.67). A second batch was mechanically alloyed (MA) with 20 Vol% TiC using the same milling parameters.

Table 2: Types of milling (AT = as-atomized, MM = mechanically milled, MA = mechanically alloyed)

Type	Vol% TiC	t / min
AT	0	0
MM	0	200
MA	20	200

All powders were consolidated in a DR. SINTER SPS1050 device (Sumitomo Coal & Mining, now SPS Syntex Inc.) with graphite dies. Disks with $d = 45$ mm and $h = 13$ mm were obtained. The heating rate was 75 K/min up to the sintering temperature of 1100 °C. The temperature was measured by a pyrometer. According to a preliminary calibration carried out using a thermocouple inside the die, closer to the sample, a temperature of 1080 °C measured by the pyrometer corresponds to an actual temperature of 1100 °C. A pressure of 60 MPa was applied at a temperature of 570 °C. The sintering time was 30 min, followed by free cooling (initially approx. 65 K/min).

3

The heat treatment consisted of austenitizing at 1020 °C for 15 min in vacuum. The specimens were quenched in a stream of 5 bars nitrogen and tempered twice at 550 °C for 2 h.

The Archimedes principle according to ASTM B962 [16] was applied to measure the density ϱ of the specimens. Young's modulus E and Poison's ratio μ were calculated by the density and the longitudinal and transversal sound wave velocities (v_l and v_t) according to DIN EN 843-2 [17]:

$$E = \varrho \frac{3v_\text{l}^2 v_\text{t}^2 - 4v_\text{t}^4}{v_\text{l}^2 - v_\text{t}^2} \tag{1}$$

$$\mu = 0.5 \frac{v_\text{l}^2 - 2v_\text{t}^2}{v_\text{l}^2 - v_\text{t}^2} \tag{2}$$

The sound wave velocities were measured with ultrasonic transducers by the pulse-echo technique. Vickers hardness measurements (HV10) were performed in an Emco-Test M4U-025 hardness tester with an indentation load of 10 kgf which was applied for 10 to 15 s according to ASTM E92 [18].

Modified disk-shaped compact tension (DCT) specimens were obtained from the sintered and heat treated discs by electric discharge machining, see Fig. 1. The upper and lower part was cut in order to achieve a height $D^* = 39.5$ mm instead of $D = 45$ mm and to use existing clevis grips for ordinary CT specimens with $B = 12.7$ mm.
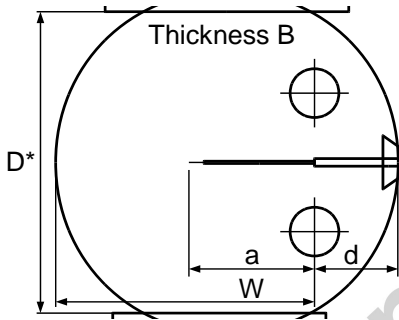

Fig. 1: Geometry of the modified DCT specimen: $B = 12.7$ mm, $a/W \approx 0.5$, $W = 33.5$ mm, $D^* = 39.5$ mm, $d = 11$ mm.

The modified geometry is not in accordance with the ASTM E 399 standard [19]. However, a FEM analysis of the stress intensity factor (SIF) revealed that the SIF calculated with Eq. 3 from ASTM E 399 results in a small error of $\leq 0.3\%$ compared to the actual SIF. Hence, an analysis according to ASTM E 399 was appropriate with the modified geometry.

$$K = \frac{F}{B\sqrt{W}} \cdot f\left(\frac{a}{W}\right) \tag{3}$$

where:

$$f\left(\frac{a}{W}\right) = \frac{\left(2 + \frac{a}{W}\right)\left(0.886 + 4.64\frac{a}{W} - 13.32\left(\frac{a}{W}\right)^2 + 14.72\left(\frac{a}{W}\right)^3 - 5.6\left(\frac{a}{W}\right)^4\right)}{\left(1 - \frac{a}{W}\right)^{1.5}} \tag{4}$$

The specimens were fatigue precracked up to a relative crack length $a_0/W \approx 0.5$. The drop in resonance frequency controlled the reduction of load during precracking. The maximum SIF in the last precracking step was ≤ 6 MPa m$^{0.5}$ for all materials. The precracked specimens were tested in a Zwick 1476 universal testing machine under cross head control and a displacement rate of 0.15 mm/min. A schematic of the experimental set-up is shown in Fig. 2.
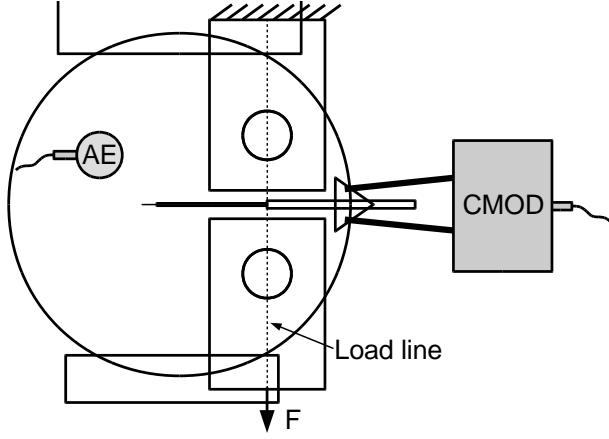

Fig. 2: Schematic of the experimental set-up. Crack mouth opening displacement (CMOD) is measured at integral knife edges. Acoustic emissions (AE) were detected by sensor near the crack tip of the specimen.

At the integral knife edges, the crack mouth opening displacement ($CMOD$) was measured. Furthermore, the plastic part of the critical crack tip opening displacement, $CTOD_{c,pl}$, was determined [20]:

$$CTOD_{c,pl} = \frac{0.46(W-a_0) \cdot CMOD_{c,pl}}{0.54a_0 + 0.46W + d} \tag{5}$$

Here, $CMOD_{c,pl}$ is the plastic part of the $CMOD$ at the critical point. The distance d between the knife edges and the load line was defined in Fig. 1. The elastic part of $CTOD_c$ was not calculated because it is just proportional to K_{Ic}^2.

Acoustic emissions generated at the crack tip were measured by an AE transducer (type PICO, Physical Acoustic Corporation, PAC), see Fig. 2. Between the specimen and the AE transducer, an Al_2O_3 plate served as a wave guide and as an electric insulation. A preamplifier (type PAC 2/4/6) with an amplification of 60 dB and a bandwidth of 10–900 kHz was applied. The signal was then digitized continuously by an 18 bit PCI-2 data acquisition board (PAC) with a sample rate of 2 MHz. Furthermore, a bandpass filter between 20 kHz and 1 MHz was applied. AE signals above a threshold level of 150 mV (noise level 50 mV) were counted as events and analyzed with respect to their energy. The event energy EE was calculated as follows:

$$EE = \frac{1}{T} \int_0^T U(t)^2 \mathrm{d}t \tag{6}$$

Where T – is the length of the recorded event and U is amplified voltage of the transducer. This voltage is proportional to the displacement at the specimen's surface, which is, in turn, a measure for the displacement at the AE source. Since the energy of an oscillation is

proportional to its squared amplitude, EE is a measure of the energy of each acoustic event. Next, the AE cumulative energy CE was calculated for the whole duration of the experiment:

$$CE = \sum_{i=1}^{n} EE_i \tag{7}$$

Where n is the number of AE events during the experiment.

The fracture surfaces of the broken specimens were investigated on the one hand by means of optical microscopy in order to measure the initial crack length, a_0, and one the other hand by means of scanning electron microscopy (SEM) in order to evaluate the effect of the microstructure on the crack resistance. A typical broken specimen is shown in Fig. 3.
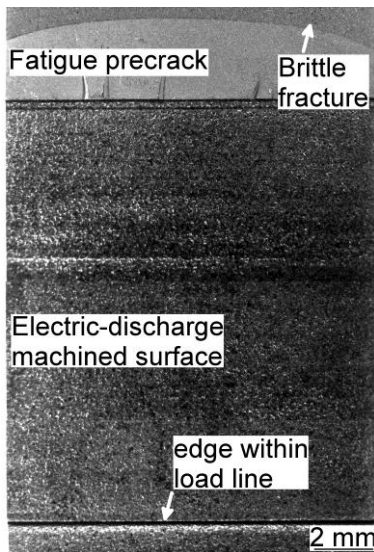

Fig. 3: Typical broken specimen (here: AT) with machined notch, fatigue precrack and brittle fracture. The edge within the load line was used to measure a_0.

Additionally, the roughness of the fracture surfaces was measured by means of white light interferometry (type SMS, Breitmeier). The microstructure was analyzed by optical microscopy and SEM after standard metallographic preparation and chemical etching (Nital 2%).

3. Results

3.1. Densification
Previous studies proved the suitability of the sintering parameters used for the present samples [5, 21]. However, the diameter of the sintered disk was larger than in those studies ($D = 20$ and 30 mm). Hence, the densification was briefly checked.
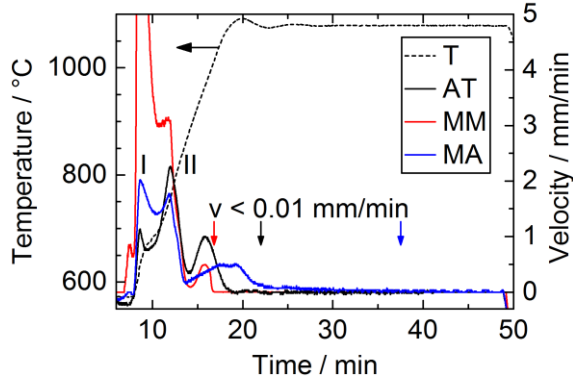
6

Fig. 4. Densification of different powders.

Fig. 4 shows the densification rate of the different powders, measured by punch velocity of the SPS device. The temperature/time regime varied insignificantly between different sintering batches (< 0.2 %), hence only one curve is reported. The first densification peak (I in Fig. 4) appeared during the application of pressure and corresponds to the rearrangement of powder particles. With further temperature increase, the densification due to the sintering proceeded. This process was superimposed to the ferrite/austenite transformation (II in Fig. 4) at approximately 890 °C (14 min). As discussed elsewhere, this transformation reduced the sintering speed [2]. In all cases the densification rate dropped down to values close to zero, meaning that, apparently, densification goes to completion during SPS. For the MM material, this condition was achieved still during the heating phase, at about 1010°C. On the other hand, densification becomes more and more difficult for the MA material due to the lower compressibility of the milled powder strengthened by the hard particles dispersion. The relatively low surface area of the AT powder particles compared to the MM powder resulted in slower densification. The AT powder showed no further densification just after reaching T_{sinter} whilst MA achieved this goal after 19 min at T_{sinter}.

The density measurements confirm a very high value for AT (99.2%) and lower values for MM (98.3%) and MA (97.8%), respectively (Fig. 5). Porosity has a detrimental effect on the Young's modulus of UFG metals as evidenced by the equation of Spinner et al. [22]:

$$E = E_0(1 - f_1 P + f_2 P^2) \tag{3}$$

where E is the reduced modulus, E_0 is the reference modulus, f_1 and f_2 are parameters equal to 1.9 and 0.9 [23], respectively, and P is the porosity. Looking at the measured porosities of MM and AT, the ratio E_{MM}/E_{AT} is 0.983. This value is in very good agreement with the E_{MM}/E_{AT} ratio (0.986) calculated by the measured Young's moduli ($E_{MM} = 211$ GPa, $E_{AT} = 214$ GPa). On the other hand, the higher E value of MA is due to the higher Young's modulus of TiC (460 GPa [24]).
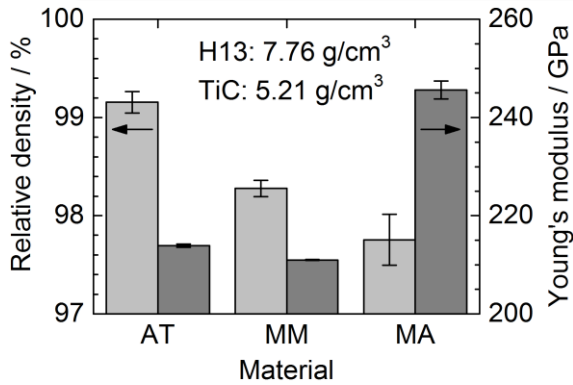
7

Fig. 5: Relative density and Young's modulus for different materials. Theoretical densities: H13: 7.76 g/cm^3, TiC: 5.21 g/cm^3 [25], MA: 7.25 g/cm^3

The microstructure of heat treated AT consists of tempered martensite and the average grain size is 5 μm (Fig. 4a). The same microstructure is shown by MM, but its grain size is about 1 μm for about 90 % of sample: the rest is generally coarser, due to the lower strain hardening during milling (Fig. 4b) [26]. The microstructure of MA is also very fine (Fig. 4c): it has been proved that hard particles enhance the particles fragmentation as well as the strain hardening process. The size of TiC particles is refined (<1μm) and their distribution inside the mechanically alloyed areas (MA) is quite uniform. Nevertheless, some regions of H13 tool steel which are not mechanically alloyed are still evidenced.
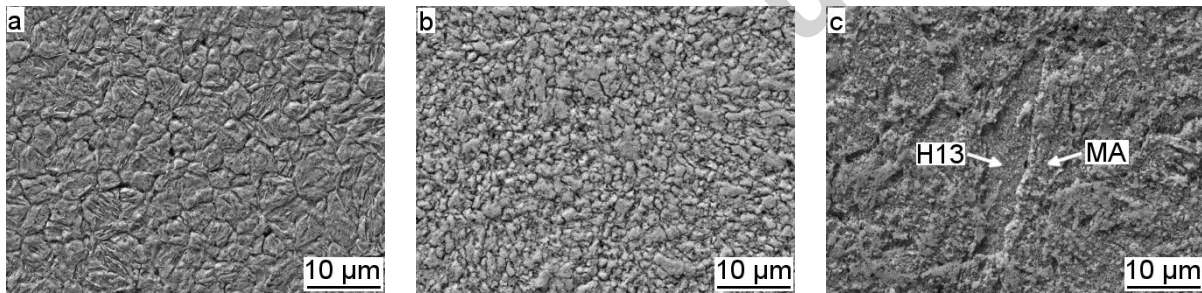

Fig. 6: Microstructure of a) AT, b) MM and c) MA tool steel

3.2. Fracture toughness and hardness

Fig. 7a shows $F/CMOD$ plots for all tested specimens. The difference in slope of the AT and MM specimens were attributed to difference in Young's modulus and small variations in a_0/W. The higher stiffness of the MA specimens was the result of the different E (246 GPa for MA, 214 GPa for AT, 211 GPa for MM). Furthermore, some of the specimens exhibited non-linear behavior. Nevertheless, valid values of K_{Ic} were determined from these specimens (Fig. 7b). Assuming a yield strength of 1000 MPa, a minimum thickness of 2 mm was required for the AT specimens to fulfill plane strain requirements of ASTM E 399. Taking the hardness of at least 640 HV10 into account, even a higher yield strength and, hence, a lower minimum thickness could be expected. In view of the limited experimental scatter, AT shows the highest fracture toughness (28 MPa m$^{0.5}$) followed by MM (21 MPa m$^{0.5}$) and MA (14 MPa m$^{0.5}$).
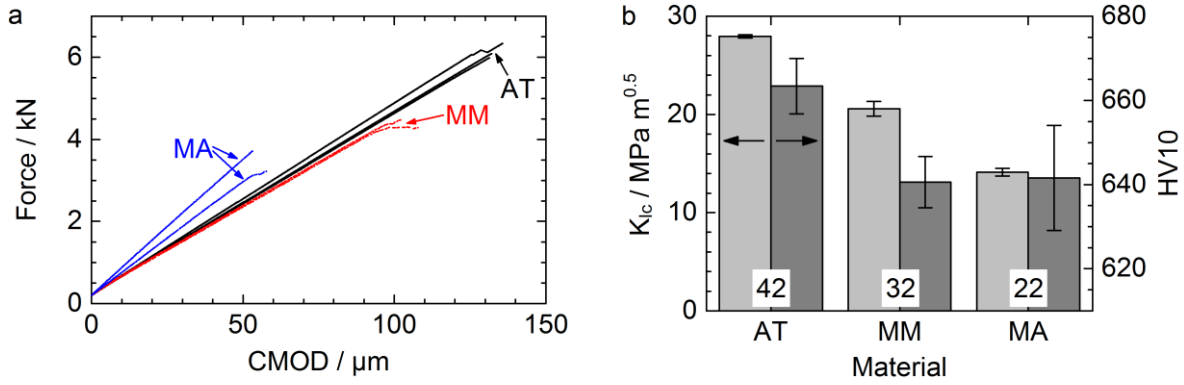
8

Fig. 7: (a) Force-CMOD curves for different materials and (b) their respective fracture toughness and hardness. The numbers show the ratio of fracture toughness to hardness ($1000 \cdot K_{Ic}/HV10$).

As expected, the plane strain fracture toughness values (K_{Ic}) determined in the present investigation are well below the apparent fracture toughness (K_{app}) from previous studies [4, 21], which is in good agreement with the higher stress triaxiality due to the lower notch tip radius [6]. Furthermore, the fracture toughness of the AT specimens reflects the literature values [7, 9].

Quite surprisingly, the hardness of the MM and MA specimens is lower than that of AT, confirming that porosity hides the potential strengthening induced by grain refinement, strain and dispersion hardening. The role of porosity is also reflected in the similar hardness of MM and MA and contributes to the lower K_{Ic} values of MM and MA than AT. The decreasing ratio $K_{Ic}/HV10$ (white boxes in Fig. 7b) indicates the cumulative embrittlement of the steel undergoing MM and MA.
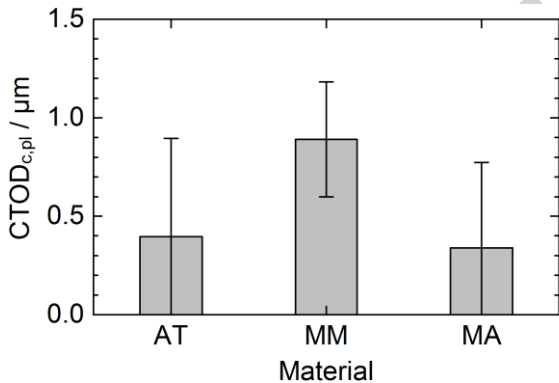

Fig. 8: Plastic part of the critical $CTOD$ for different materials.

The non-linear behavior of the $F/CMOD$ plots (Fig. 7a) is reflected by $CTOD_{c,pl}$ of the three materials, see Fig. 8. The highest plastic crack tip opening before fracture was observed for the MM specimens. Since some of the AT and MA specimens showed nearly pure linear-elastic behavior until fracture, a large scatter was found.

9

3.3. Damage evolution

Analysis of SIF and AE signals

Fig. 9a-c shows the K_I / $CMOD$ trace and the corresponding (cumulative) AE spectral energy (CE) for all specimens. They exhibited a slight increase of the AE signal for $CMOD \lesssim$ 100 µm (AT), $CMOD \lesssim$ 90 µm (MM) and $CMOD \lesssim$ 45 µm (MA). At higher $CMOD$, the AE spectral energy exhibited a pronounced transition to a steeper slope.
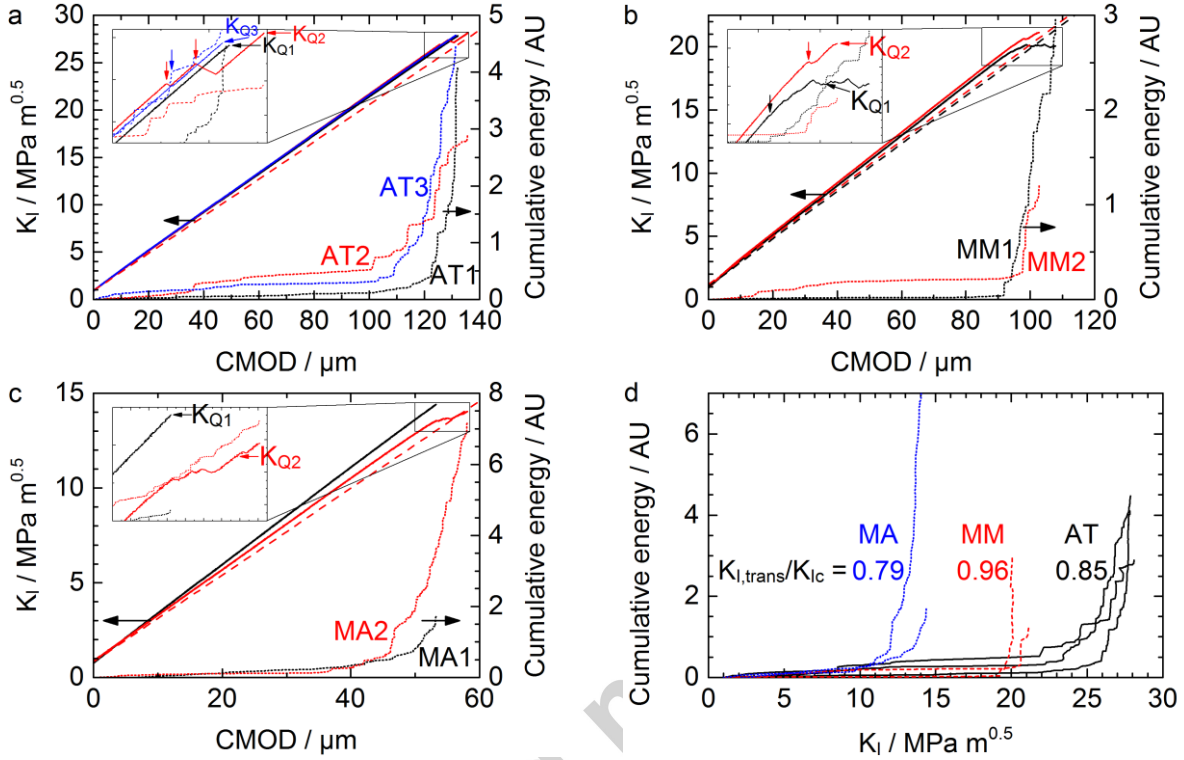

Fig. 9: Analysis of acoustic emissions for different materials. (a-c) The 95 % secants are given by dashed lines for specimens, which have small amounts of non-linear behavior. (d) Numbers indicate the transition between slight and steep increase of the AE spectral energy in terms of $K_{I,trans}/K_{Ic}$. AU: arbitrary units.

At the instant of pop-ins, which were only observed after this transition, high-energy AE signals were detected. This leads to kinks in the CE / $CMOD$ trace. This observation is in accordance with the characteristics of the applied AE sensor. The used type of sensor is very sensitive to cleavage fracture events, but less sensitive to AE generated during plastic deformation [27]. Local cleavage fractures result in damage of the uncracked material. At a certain degree of damage, the material eventually fails by unstable fracture.

Fracture events resulting in high-energy AE signals were not necessarily linked with pop-ins. Selected events are indicated by vertical arrows. However, even small pop-ins (insignificant according to ASTM E 1820) generate high-energy AE signals. Since the K_I / $CMOD$ trace is not sensitive for small fracture events, the analysis of the damage evolution is clearly enhanced by the AE signal analysis.

The non-linear behavior of the $K_I/CMOD$ trace, shown by MM1 (Fig. 9b) and MA2 (Fig. 9c), corresponds to a significantly higher increase of CE.

10

In Fig. 9a and b, initial transients at low loads ($K_I < 10$ MPa$\sqrt{m}$) are coherent with the higher CE for specimens AT2 and MM2. These AE events probably originate from interactions between the specimen and the grips. Since the tests started at loads below the precracking load, effects of first crack opening after fatigue precracking were also assumed to emit some acoustic signals.

The arrows in Fig. 9a-c indicate the conditional fracture toughness values ($K_{Q1}, K_{Q2}, \dots$) for each specimen, determined either by the force maximum or by the intersection with the 95 % secant. As stated above, all K_Q values were valid K_{Ic} values.

Fig. 9d shows a comparison of CE vs. K_I for the different materials. AT specimens revealed a relatively smooth increase of the AE cumulative energy up to fracture. For the AT and MA specimens, the increase starts at approximately $0.85 K_{Ic}$ and $0.79 K_{Ic}$, respectively. The steepest increase was observed for the MM specimens above $0.96 K_{Ic}$ confirming that the damage attributed to cleavage fracture evolves just before the final fracture. In contrast, such damage occurs much earlier in the MA specimens due to TiC particles acting as stress concentration sites. The reason for the different damage evolution will be further discussed below.

Fractographic analysis

The fracture surfaces shown in Fig. 10 demonstrate different crack growth mechanisms. The AT specimens (Fig. 10a and b) exhibited localized ductile fracture (DF), which was characterized by dimples, near the precrack tip. After a crack growth of about 20 μm, only very limited traces of ductile fracture were observed and unstable cleavage fracture (CF) prevailed, in agreement with the linear trend of K_I (Fig. 8). CF was characterized by flat facets, some of them with river patterns.

In contrast, nearly pure microductile fracture (DF) was observed for the MM specimens (Fig. 10c and d). Only some islands of cleavage fracture (CF) could be detected. The crack propagation direction was perpendicular to the long axis of original mechanically milled particles, i.e., perpendicular to the pressing direction during sintering. Some delamination is present, due to the interparticle nucleation of secondary cracks, perpendicular to the main one. This *crack division* effect should be reflected in increased toughness [15]. Moreover, delamination modifies the local stress state decreasing the stress triaxiality. Therefore, further plastic deformation can be expected before failure, explaining the occurrence of microductile fracture. Despite the potential benefits by these two toughening mechanisms, the fracture toughness of MM is lower than that of AT.

The MA specimens showed no ductile fracture, see Fig. 10e. Most of the cleavage fracture facets were very fine. The arrow in Fig. 10f indicates a relatively large cleavage fracture facet. Additionally, some aggregations of TiC were observed.
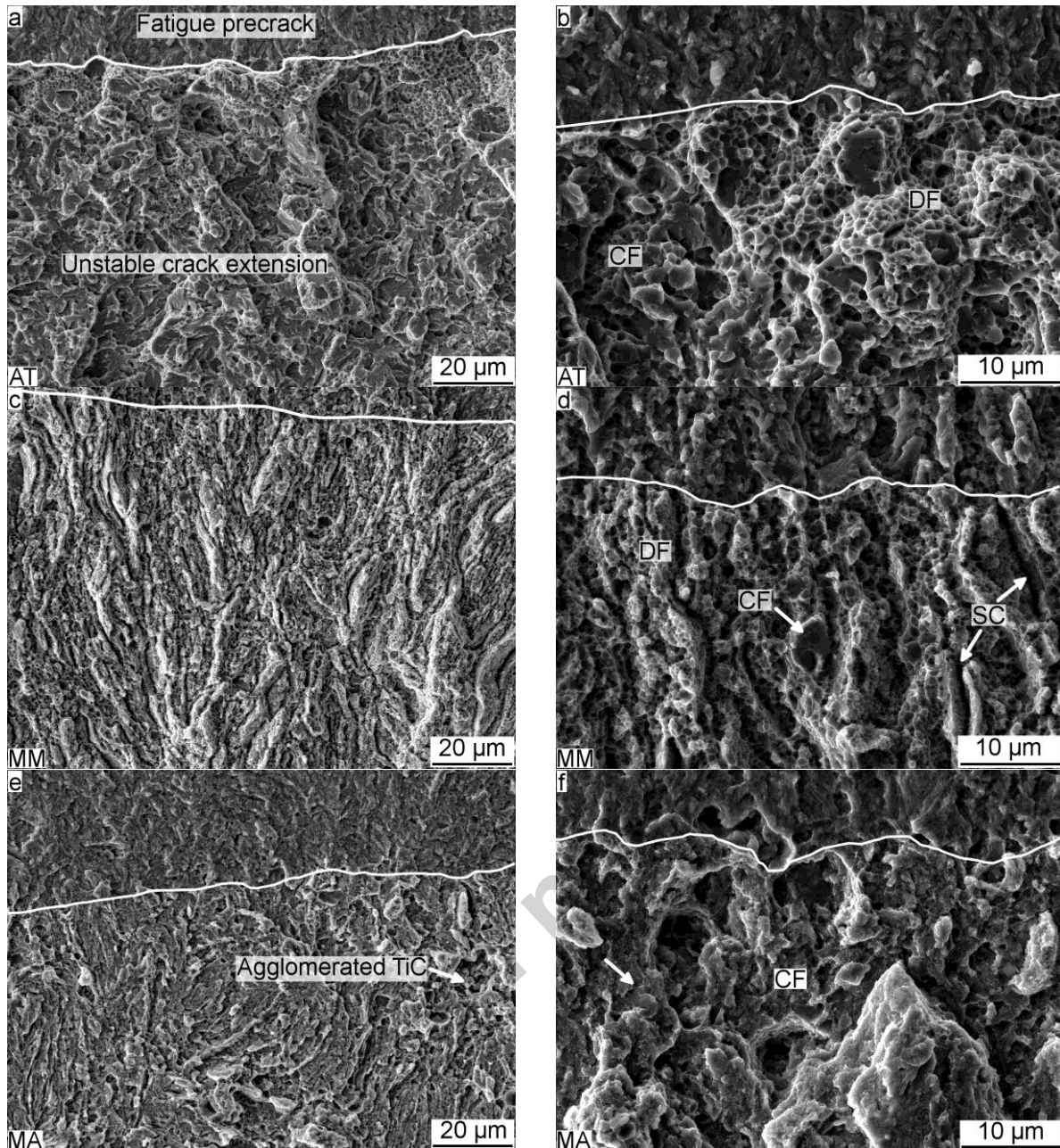
Fig. 10: Fracture surfaces showing different amounts of cleavage fracture. The fatigue precrack is above the white line for all micrographs. DF - ductile fracture; CF - cleavage fracture; SC - secondary cracks.

The crack paths of the different materials are shown in Fig. 11. The AT specimen shows higher amount of crack path deflection than the MM specimen. Crack path deflection or crack path division was also observed for the MA specimen. However, these toughening mechanisms were mostly associated with large H13 particles. Regions with a MA microstructure exhibited nearly no deflection of the crack path. From the micrographs in Fig. 11, the crack path deflection can only be described qualitatively. However, these observations were quantitatively supported by the results of the roughness measurement in Table 3. The AT and MA specimens revealed the highest and lowest roughness, respectively.
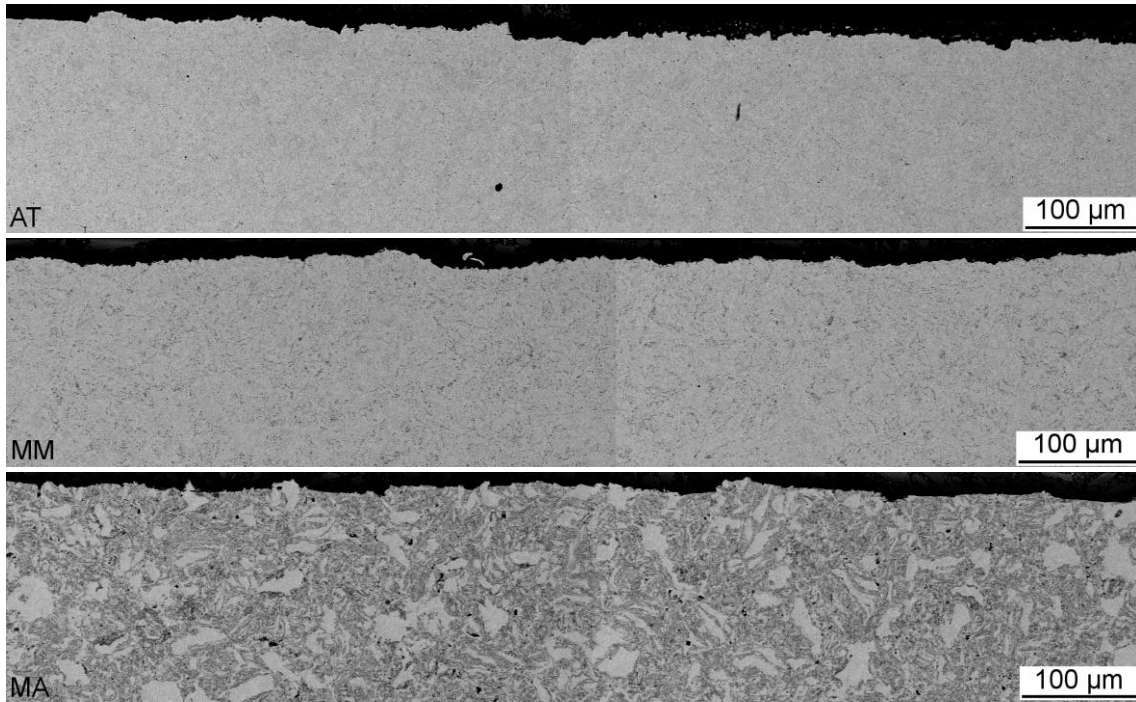
12

Fig. 11: Crack paths of the different materials in the crack growth direction

Table 3: Roughness of fracture surfaces in terms of R_a and R_z.

Material	R_a / µm	R_z / µm
AT	2.6 ± 0.2	19.2 ± 2.5
MM	2.0 ± 0.0	14.2 ± 1.3
MA	1.5 ± 0.1	12.9 ± 1.2

4. Discussion

Dislocation motion is characterized by low-frequency acoustic emissions (100−300 kHz) [28], whereas higher frequencies of about 500−625 kHz are observed for cleavage fracture of martensite [29]. The PICO AE transducer has a relatively low sensitivity at frequencies below 300 kHz [30]. At higher frequencies of about 400−600 kHz this transducer has a much higher sensitivity. Hence, this transducer is very sensitive to cleavage fracture events but less sensitive to plastic deformation. Furthermore, the threshold based processing of the signal allows to detect the transient phenomena, e.g. cleavage fracture. Smooth low amplitude signals such as AE from plastic deformation are not considered.

In Fig. 9d, the AT and MA (especially MA1) specimens revealed a relatively smooth increase of the AE cumulative energy up to fracture. This was attributed to the damage by local cleavage fracture observed by fracture surface analysis, see Fig. 10a and c. This local cleavage fracture occurred at grains with favorable orientation. In the MA specimens, fracture of large TiC agglomerates lead to additional damage before fracture. Consequently, the MA specimens revealed a pronounced increase of the AE spectral energy at relatively small K_I/ K_{Ic}. The non-linear behavior of specimen MA2 (Fig. 9c) in terms of the K_I / $CMOD$ trace was attributed to local cleavage cracks that were stopped by large H13 particles (see Fig. 11).

13

For the MM specimens, this transition of the AE cumulative energy occurred shortly before fracture ($K_I \approx 0.96 K_{Ic}$, Fig. 9d). Considering the fracture surfaces (Fig. 10c and d), local cleavage fracture facets and secondary cracks resulted only in small load drops (pop-ins, also found in [31]) and a very limited damage before fracture. This is attributed to the high cleavage fracture strength in fine grains [32]. On the other hand, a small amount of large grains is still present after the mechanical milling process and the SPS treatment [4, 26], which will contribute to localized cleavage events before final fracture (Fig. 9b).

The fracture toughness is not only affected by the damage evolution, but also by the possible crack path. The relatively high K_{Ic} of the AT specimens was attributed to both the high density and the relatively coarse microstructure. The low pore volume fraction results in less stress concentration from internal notches. Furthermore, the relatively coarse grains result in pronounced crack path deflection, which is a toughening mechanism. In contrast, the internal notch effect is higher for both the MM and MA specimens due to their higher porosity. Hence, the ductile fracture, which was also reflected by the relatively high plastic part of the $CTOD_c$ (Fig. 8), did not compensate the detrimental effect of the porosity in the MM specimens. In the MA specimens, coarse TiC agglomerates, which were not fully broken during the MA process, act as additional stress concentration sites. Hence, the cleavage fracture strength was exceeded.

5. Summary and conclusions

The effect of the processing route and the addition of 20 Vol% TiC particles on the fracture toughness of the hot work tool steel AISI H13 was investigated. The damage evolution was studied by the analysis of acoustic emissions and fracture surface analyses. The main results can be summarized as follows:

- Irrespective of the processing route, the SPS process produced nearly dense material. The highest density was achieved for the as-atomized powder, the lowest for the mechanically alloyed powder.
- Mechanical milling of AISI H13 resulted in a fine microstructure and lower fracture toughness compared to the as-atomized powder. This was explained by a higher porosity and a lower amount of crack path deflection.
- The addition of 20 Vol% TiC particles and mechanical alloying resulted in the lowest fracture toughness. This behavior was attributed to the relatively low density. Moreover, mechanical alloying resulted in an insignificant amount of crack path deflection. TiC agglomerates, which were not fully broken during the milling process, acted as stress concentration sites.

14

analysis, Annette Ludwig for roughness measurement and Patrick Schlenz and Anna Freigang for specimen preparation.

6. References

[1] Roberts, G. A.; Krauss, G.; Kennedy, R.: Tool steels. Materials Park, OH: ASM International (1998).

[2] Pellizzari, M.; Fedrizzi, A.; Zadra, M.: Influence of processing parameters and particle size on the properties of hot work and high speed tool steels by Spark Plasma Sintering, *Mater. Design,* 32 (2011) 4, 1796–1805. DOI: 10.1016/j.matdes.2010.12.033.

[3] Pellizzari, M.; Fedrizzi, A.; Zadra, M.: Spark Plasma co-Sintering of hot work and high speed steel powders for fabrication of a novel tool steel with composite microstructure, *Powder Technology,* 214 (2011) 3, 292–299. DOI: 10.1016/j.powtec.2011.08.024.

[4] Pellizzari, M.; Fedrizzi, A.; Zadra, M.: Spark plasma co-sintering of mechanically milled tool steel and high speed steel powders, *Materials,* 9 (2016) 6, 482. DOI: 10.3390/ma9060482.

[5] Fedrizzi, A.: Production of steel matrix composites by mechanical milling and spark plasma sintering, Ph.D. Thesis, University of Trento (2013).

[6] Lee, B.-W.; Jang, J.-i.; Kwon, D.: Evaluation of fracture toughness using small notched specimens, *Mat. Sci. Eng. A,* 334 (2002) 1–2, 207–214. DOI: 10.1016/S0921-5093(01)01804-4.

[7] Okorafor, O. E.: Fracture toughness of M2 and H13 alloy tool steels, *Mater. Sci. Technol.,* 3 (1987) 2, 118–124. DOI: 10.1179/mst.1987.3.2.118.

[8] Qamar, S. Z.; Sheikh, A. K.; Arif, A.F.M.; Pervez, T.: Regression-based CVN–KIC Models for hot work tool steels, *Mat. Sci. Eng. A,* 430 (2006) 1-2, 208–215. DOI: 10.1016/j.msea.2006.05.103.

[9] Asdrúbal Valencia, G.; Worzala, F. J.: Fracture toughness study of 5% Cr-Mo-V steel, *Rev. Lat. Am. Met. Mater.,* 2 (1982) 2, 97–106.

[10] Leskovšek, V.: Correlation between the K_{Ic}, the HRc and the Charpy V-notch test results for H11/H13 hot-work tool steels at room temperature, *Steel Res. Int.,* 79 (2008) 4, 306–313. DOI: 10.1002/srin.200806355.

[11] Pezzotti, G.; Okamoto, Y.; Nishida, T.; Sakai, M.: On the near-tip toughening by crack-face bridging in particulate and platelet-reinforced ceramics, *Acta Mater.,* 44 (1996) 3, 899–914. DOI: 10.1016/1359-6454(95)00250-2.

[12] Ingham, T.; Stott, A. L.; Cowan, A.: Acoustic emission characteristics from steels, Part 2: Acoustic measurements from fracture toughness tests, *Int. J. Pres. Ves. Pip.,* 3 (1975) 4, 267–293. DOI: 10.1016/0308-0161(75)90010-1.

[13] Lambert, A.; Garat, X.; Sturel, T.; Gourgues, A.F.; Gingell, A.: Application of acoustic emission to the study of cleavage fracture mechanism in a HSLA steel, *Scripta Mater.,* 43 (2000) 2, 161–166. DOI: 10.1016/S1359-6462(00)00386-9.

[14] Roy, H.; Parida, N.; Sivaprasad, S.; Tarafder, S.; Ray, K. K.: Acoustic emissions during fracture toughness tests of steels exhibiting varying ductility, *Mat. Sci. Eng. A,* 486 (2008) 1-2, 562–571. DOI: 10.1016/j.msea.2007.09.036.

[15] Hohenwarter, A.; Pippan, R.: Fracture and fracture toughness of nanopolycrystalline metals produced by severe plastic deformation, *Philos. Trans. R. Soc. London Ser. A,* 373 (2015) 2038, 20140366. DOI: 10.1098/rsta.2014.0366.

[16] ASTM B962-15, 2015: Standard test methods for density of compacted or sintered powder metallurgy (PM) products using Archimedes' principle.

[17] DIN EN 843-2, 2007: Hochleistungskeramik – Mechanische Eigenschaften monolithischer Keramik bei Raumtemperatur – Teil 2: Bestimmung des Elastizitätsmoduls, Schubmoduls und der Poissonzahl.

[18] ASTM E92-82, 1997: Standard Test Method for Vickers Hardness of Metallic Materials.

[19] ASTM E 399, 2012: Standard test method for linear-elastic plane-strain fracture toughness K_{Ic} of metallic materials.

[20] ISO 12135, 2002: Metallic materials – Unified method of test for the determination of quasistatic fracture toughness.

[21] Deirmina, F.; Pellizzari, M.; Federici, M.: Production of a powder metallurgical hot work tool steel with harmonic structure by mechanical milling and spark plasma sintering, *Metall. Mater. Trans. A,* 48 (2017) 4, 1910-1920. DOI: 10.1007/s11661-017-3957-5.

[22] Spinner, S.; Knudsen, F. P.; Stone, L.: Elastic constant- porosity relations for polycrystalline thoria, *J. Res. Natl. Bur. Stand., Sect. C.,* 67C (1963) 1, 39–46. DOI: 10.6028/jres.067C.005.

[23] Meyers, M. A.; Mishra, A.; Benson, D. J.: Mechanical properties of nanocrystalline materials, *Prog. Mater. Sci.,* 51 (2006) 4, 427–556. DOI: 10.1016/j.pmatsci.2005.08.003.

[24] Török, E.; Perry, A. J.; Chollet, L.; Sproul, W. D.: Young's modulus of TiN, TiC, ZrN and HfN, *Thin Solid Films,* 153 (1987) 1-3, 37–43. DOI: 10.1016/0040-6090(87)90167-2.

[25] Sherif El-Eskandarany, M.: Structure and properties of nanocrystalline TiC full-density bulk alloy consolidated from mechanically reacted powders, *J. Alloy Compd.,* 305 (2000) 1-2, 225–238. DOI: 10.1016/S0925-8388(00)00692-7.

[26] Fedrizzi, A.; Pellizzari, M.; Zadra, M.; Marin, E.: Microstructural study and densification analysis of hot work tool steel matrix composites reinforced with TiB_2 particles, *Mater. Charact.,* 86 (2013), 69–79. DOI: 10.1016/j.matchar.2013.09.012.

[27] Kietov, V.; Henschel, S.; Krüger, L.: Study of dynamic crack formation in nodular cast iron using the acoustic emission technique, *Eng. Fract. Mech., (*2017). DOI: 10.1016/j.engfracmech.2017.07.009.

[28] Pomponi, E.; Vinogradov, A.: A real-time approach to acoustic emission clustering, *Mech. Syst. Signal Pr.,* 40 (2013) 2, 791–804. DOI: 10.1016/j.ymssp.2013.03.017.

[29] Khamedi, R.; Fallahi, A.; Refahi Oskouei, A.: Effect of martensite phase volume fraction on acoustic emission signals using wavelet packet analysis during tensile loading of dual phase steels, *Mater. Design,* 31 (2010) 6, 2752–2759. DOI: 10.1016/j.matdes.2010.01.019.

[30] Physical acoustics corporation (2011): Product data sheet PICO sensor. Available online: http://www.physicalacoustics.com/content/literature/sensors/Model_PICO.pdf.

[31] Hohenwarter, A.; Pippan, R.: Fracture of ECAP-deformed iron and the role of extrinsic toughening mechanisms, *Acta Mater.,* 61 (2013) 8, 2973–2983. DOI: 10.1016/j.actamat.2013.01.057.

[32] Petch, N. J.: The cleavage strength of polycrystals, *J. Iron Steel Inst.,* 174 (1953) 5, 25–28.